Journal of Alloys and Compounds 855 (2021) 157337

Contents lists available at ScienceDirect

Journal of Alloys and Compounds

journal homepage: http://www.elsevier.com/locate/jalcom

DFT and experimental investigations on the photocatalytic activities of NiO nanobelts for removal of organic pollutants

Narasimharao Kitchamsetti [a], Mrunmay S. Ramteke [a], Sachin R. Rondiya [b], Sameena R. Mulani [a], Madhuri S. Patil [a], Russell W. Cross [b], Nelson Y. Dzade [b], Rupesh S. Devan [a, *]

[a] Discipline of Metallurgy Engineering & Materials Science, Indian Institute of Technology Indore, Simrol, Indore 453552, India
[b] School of Chemistry, Cardiff University, Cardiff, CF10 3AT, Wales, United Kingdom

ARTICLE INFO

Article history:
Received 10 August 2020
Received in revised form
6 September 2020
Accepted 24 September 2020

Keywords:
NiO nanobelt
DFT
Dye degradation
Photocatalyst
Organic pollutant
Wastewater treatment
etc

ABSTRACT

NiO nanobelts synthesized using the hydrothermal method are explored for photocatalytic degradation of organic pollutants like RhB, MO, MB, and CV. The XPS analysis confirmed the formation of the stoichiometric NiO nanobelts. Few micrometer long cubic crystalline NiO nanobelts of the average thickness of ~75 nm delivered a bandgap of 4.07 eV. The FTIR studies revealed that the mesoporous NiO nanobelts delivered stable photocatalytic activities after controlled irradiation under a xenon lamp. The kinetic studies showed the 79.1, 82.7, 76.7, and 89% degradation of MO, MB, CV, and RhB after 140 min at the rate constants (k) of 0.007, 0.008, 0.009, and 0.012 min^{-1}, respectively. Complementary first-principles Density Functional Theory (DFT) and scavenging studies revealed the chemical picture and influence of the O_2^-, and photogenerated H^+ from NiO nanobelts in the photocatalytic degradation of organic dyes. These studies corroborate the use of the NiO nanobelts in the stable and eco-friendly photocatalytic degradation activities of a wide range of organic pollutants.

1. Introduction

In recent years, water, an essential part of our eco-system, is polluted with the advancement of modern manufacturing, textile, and energy industries. The vast numbers of artificial dyes useful for paper, pulp cloth, textile, leather treatment, print industries [1,2] are produced massively (i.e., ~7,00,000 tons) every year [3]. Even though these dyes are an essential component of the industries, unfortunately, drained directly in the water/soil after industrial processes without proper treatment. Their toxic nature is affecting the biological cycle of the environment, and hence directly distressing on human beings [4]. The layers of the dye molecules formed on the water surface slabs the sunlight and interrupt the photosynthesis and respiration of organisms in the water. Moreover, the dyes degrade the soil strength and directly extinguish the farming wealth, which causes severe health complications. Therefore, removal of the dyes from the water resources is the immediate needs of society. Various methods such as adsorption, coagulation, membrane filtration, reverse osmosis, ozonation, sedimentation, advanced oxidation processes, and photocatalytic degradation [5] have been adopted for the separation of the organic dyes from wastewater. However, the photocatalytic degradation, known as one of the green technologies, where solar energy is involved directly, is attracting the scientific and industrial community for highly effective elimination or mineralization of synthetic organic dyes.

Owing to the flexibility in tailoring the morphology and bandgaps, the metal oxide nanomaterials have been considered as competent photocatalysts to remove synthetic dyes under different conditions. However, the most effective and efficient photocatalyst is expected to be non-toxic, highly stable, and reusable. So far, metal oxides of Ti, Zn, Mn, Cu, Co, and Ni [6,7] are explored extensively to extract the dyes from the water. The non-toxic nature and cheaper costs lead researchers to consider the TiO_2 and ZnO in the first place. However, the high mobility (i.e., $\mu = 10^{-5}$ cm^2/V, and 10^2 cm^2/V, respectively) and large bandgap (i.e., $E_g = 3.2-3.4$ eV) of TiO_2 and ZnO have restricted their photocatalytic degradation rate [8]. Even though CuO and Co_3O_4 hold the high ability of dye removal in the visible light range, the fast recombination rate of

* Corresponding author.
E-mail address: rupesh@iiti.ac.in (R.S. Devan).

https://doi.org/10.1016/j.jallcom.2020.157337

electron-hole pairs has obstructed the catalytic behavior [9,10]. Likewise, various crystallographic polymorphs of multifunctional MnO_2 such as α, β, γ, and δ type delivered diversified photocatalytic properties. However, relatively weaker magnetic properties hindered their separation from the treated water, and hence limiting their practical applications [11]. The main features to be efficient photocatalysts are appropriate morphology, non-toxicity, suitable bandgap, and stability. Therefore, Nickel oxide (NiO) has attracted considerable attention as efficient photocatalysts. However, more efforts are necessary to explore the variety of NiO nanostructure morphologies for photocatalytic dye degradation.

So far, different methods are employed for the synthesis of a variety of NiO nanostructures for application in solar cells [12], electrochromic smart windows [13], supercapacitor [14], gas sensing [15], and fuel cells [16], etc. Moreover, nanoparticle, nanoflakes, nanoflower, and nanospheres morphologies are explored for photocatalytic applications. NiO nanoparticles synthesized by the thermal decomposition process act as proficient photocatalysts towards the degradation of Rhodamine B (RhB) under UV light illumination [17]. Yu et al. [4] reported that the hierarchical porous NiO nanosheets prepared using chemical precipitation techniques were effective adsorbents for the removal of Congo Red (CR) pollutants from wastewater. Moreover, the cobalt substituted NiO nanoparticles synthesized by chemical co-precipitation actively degraded the Methylene Blue (MB) in the presence of natural sunlight [18]. However, to the best of our knowledge, none of the reports mentioned the utilization of porous NiO nanobelts for photocatalytic applications. In our work, we report the utilization of NiO nanobelts synthesized by the hydrothermal method for the photocatalytic removal of synthetic dyes like RhB, MB, MO, and CV, respectively. The structural, surface morphological, and photocatalytic studies suggest the excellent photocatalytic behavior of NiO nanobelts for the removal of RhB dyes.

2. Experimental techniques

2.1. A. synthesis and characterization

The perforated NiO nanobelts were synthesized on ITO coated glass substrate via the hydrothermal route. 1 M Nickel Sulfate ($NiSO_4 \cdot 6H_2O$, 99.9%, Sigma Aldrich) dissolved in the deionized water was reacted with Ethanol (C_2H_5OH, 99.9%, SRL chemicals). The pH of the solution was maintained to 12 after reacting to the aqueous ammonia solution ($NH_3 \cdot H_2O$, Extra pure, 25% SRL Chemicals) for 30 min at room temperature, and the whole solution was transferred to the autoclave consisting of cleaned ITO/glass substrates. The hydrothermal reaction was carried out for 12 h at 180 °C and allowed to cool down to room temperature, which was further washed with deionized water several times and dried. After that, the crystal structure of NiO thin film was confirmed from X-ray diffraction studies performed using D2-phase Bruker XRD equipped with a Cu Kα radiation (λ = 1.5405 Å). The surface morphological features were confirmed from field-emission scanning electron microscope (FESEM, JEOL JSM-6500F) furnished with Energy dispersive X-ray spectroscopy (EDS, Oxford instrument INCA, X-sight 7557) for elemental analysis. The chemical composition and electronic structure of NiO nanobelts were explored from X-ray photoelectron spectroscopy (XPS, Thermo Scientific Inc. K-alpha) with a microfocus monochromated Al Kα X-rays. The optical properties were investigated from UV−Vis spectra recorded on UV−Visible spectrophotometer (Shimadzu UV-2600). The photocatalytic activities of NiO nanobelts optimized on the RhB, initially, and further continued for MO, CV, MB under xenon light irradiation (λ = 100−1800 nm) in Photo-Chem Reactor. The 25, 40, and 60 mg of NiO catalyst was added in to a 10 ppm RhB, MB, CV, and MO aqueous solutions under constant stirring at room temperature. Furthermore, the mixture was stirred for 60 min to attain an adsorption-desorption equilibrium [19], and after that, the solution was photo-reacted under a Xenon lamp (300 W). The irradiated solution was tested at regular intervals using a UV−Vis spectrophotometer. The initial concentration (C_o) and concentration at reaction time t (C_t) of RhB, MB, CV, and MO dye solutions were monitored to estimate the photocatalytic dye removal rates using the formulae [20].

$$\text{Dye degradation efficiency } (\%) = \frac{C_o - C_t}{C_o} \times 100 \quad (1)$$

2.2. B. computational analysis

The first-principles density functional theory (DFT) calculations were performed using the Vienna Ab initio Simulation Package (VASP) [21]. Wherein interactions between the core and valence electrons were treated using the Project Augmented Wave (PAW) method [22]. The electronic wave functions are expanded on a plane-wave basis set with a cutoff energy of 600 eV. The conjugate-gradient algorithm used to perform geometry optimizations until the residual Hellmann−Feynman forces on all relaxed atoms reached 10^{-3} eV/Å. The electronic exchange-correlation potential was calculated using the Perdew−Burke−Ernzerhof (PBE) generalized gradient approximation (GGA) functional [23]. Long-range vdW interactions were accounted for using the Grimme DFT-D3 scheme [24]. The bulk NiO was modeled in the rock salt structure (*Fm-3m* [No. 225]) with antiferromagnetic spin ordering yielding the lattice parameter of $a = 4.209$ Å in close agreement with reported experimental data [25,26]. A 9 × 9 × 9 Monkhorst-Pack *k*-point mesh used to sample the Brillouin zone. The screened hybrid functional HSE0 [27] was used with the exchange value of 25% to predict the band gap accurately. The NiO(110) surface, created using the METADISE code [28], was used to characterize the adsorption O_2 molecule. A 5 × 5 × 1 *k*-point was used for the surface calculations. Bader charge analysis [29] was used to quantify any charge transfers between the NiO(110) surface and the O_2 molecule.

3. Results and discussion

The crystalline nature of the NiO nanobelts is confirmed from the Rietveld refinement of the XRD spectra shown in Fig. 1. The characteristic XRD peaks observed for NiO nanobelts at 2θ of 37.3 , 43.3 , 62.9 , 75.4 , and 79.4 are attributed to the (111), (200), (220), (311), and (222) diffraction peaks, respectively, and confirmed the cubic crystalline nature of NiO nanobelts (JCPDS No. 47−1049) corresponds to space group of Fm-3m. None of the peaks in the XRD spectra left unidentified. The lattice parameters obtained are a = b = c = 4.196 Å. The Bragg R-factor, R_f factor, the goodness of fit factor (GofF), χ^2 value, and x-ray density gained from Rietveld refinement are 8.73, 6.10, 2.3, 5.08, and 6.718 g/cc, respectively. This confirms that the calculated and experimental values are in good accord.

Fig. 2 (a and b) displays the surface morphological feature of NiO deposited on the ITO coated glass substrate. The porous network has grown over a larger area (Fig. 2(a)) consists of long-range NiO nanobelts (Fig. 2(b)). Each individual NiO nanobelt depicts a smooth surface and clearly visible textural boundaries. The average thickness of the few micrometer long NiO nanobelts was ~75 nm. This indicates that the porous network and long ordering of NiO nanobelts can provide plentiful trapping sites for electron, which can control the recombination of electron-hole pair and assists in

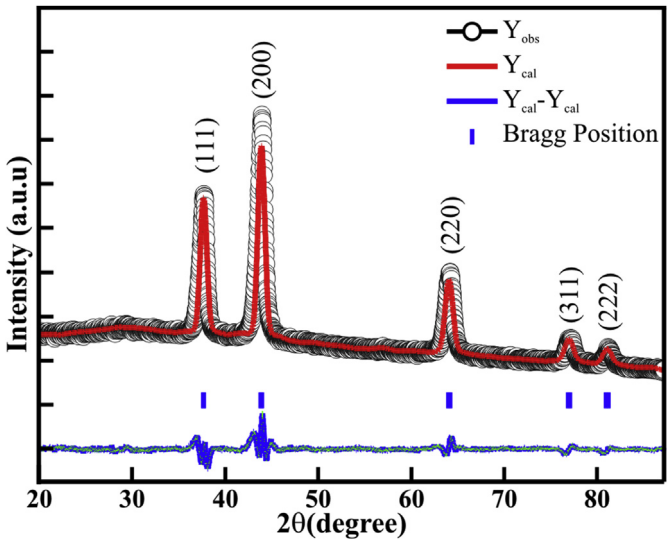

Fig. 1. Rietveld refinement of XRD pattern of NiO nanobelts.

the improvement of the dye degradation performance. Moreover, our recent nitrogen adsorption-desorption isotherm and BJH pore size distribution studies confirmed that NiO nanobelts provide a specific surface area of 40.57 m^2/g [30]. In view of this larger specific surface area and longer connection path, the NiO nanobelts are anticipated to exhibit an excellent photocatalytic activity. The EDS analysis performed on the NiO nanobelts shows the existence of Ni and O elements only and confirms that the porous network of nanobelts was composed of NiO without any impurity.

X-ray photoelectron spectroscopy was utilized for analyzing the chemical compositions and electronic states of the NiO nanobelts. Fig. 3 shows high-resolution XPS spectra of the Ni(2p) and O (1s) core levels of the NiO nanobelts. Both XPS spectra are deconvoluted with Voigt function fitting, followed by a Shirley background to precisely determine the features of Ni(2p) and O (1s). The XPS spectra of Ni(2p) core levels showing four distinct peaks identified as A, B, C, and D, and are assigned to the Ni($2p_{3/2}$) and Ni($2p_{3/2}$) core levels, and their respective shake-up satellite peaks. However, the deconvolution of the spectra shows a perfect fit for 8 peaks labeled as a, a′, b, b′, c, c′, d, and d′. These peaks consecutively located at binding energy of 856.4, 858.8, 862.4, 867.1, 874.6, 877.0, 880.7, and 885.2 eV assigned to the $Ni^{2+}(2p_{3/2})$, $Ni^{3+}(2p_{3/2})$, $Ni^{2+}(2p_{3/2})$ shakeup satellite, $Ni^{3+}(2p_{3/2})$ shakeup satellite, $Ni^{2+}(2p_{1/2})$, $Ni^{3+}(2p_{1/2})$, $Ni^{2+}(2p_{1/2})$ shakeup satellite, and $Ni^{3+}(2p_{1/2})$ shakeup satellite, respectively. The distinctly intense peak of Ni($2p_{3/2}$) and Ni($2p_{1/2}$) core levels of Ni^{2+} ions evidenced the formation of NiO nanobelts. However, it is accompanied by other peaks observed at 2.4 eV higher binding energy and assigned to the Ni^{3+} ions. However, the much higher intensity of $Ni^{2+}(2p_{3/2})$ than that of $Ni^{3+}(2p_{3/2})$ confirmed the formation of stoichiometric NiO nanobelts in larger quantities, while accompanied by an insignificant amount of Ni_2O_3 subsidiary phase [30]. The energy separation of 18.2 (±0.1) eV between the Ni($2p_{3/2}$) and Ni($2p_{1/2}$) core levels remained identical for their shake-up satellite peaks. Similarly, the broad peak of O (1s) XPS spectra deconvoluted in to two peaks located at a binding energy of 531.2 and 533.4 eV are assigned to the O (1s) core levels of the O^{2-} anions of stoichiometric NiO nanobelts, and surface contaminations or nickel hydroxide or defects sites on the surface [31–33]. Furthermore, the binding energy separation (ΔE) of 325.2 eV in the Ni($2p_{3/2}$) and O (1s) core levels is relatively smaller than that of the non-stoichiometric Ni_2O_3 (i.e., 326.2 eV), and significantly larger than 321.7 eV assigned to the metallic Ni [30].

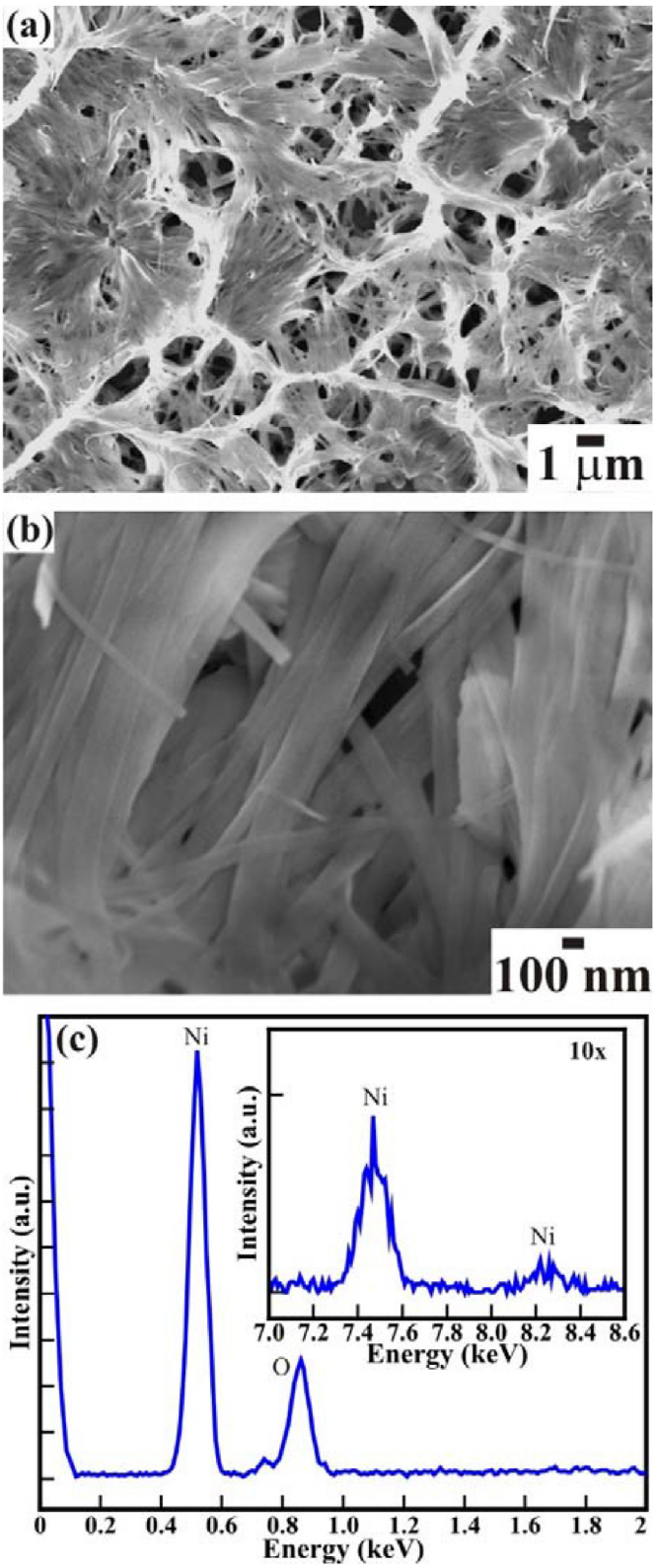

Fig. 2. Top view FESEM images showing the (a) porous network of (b) long-range NiO nanobelts. (c) EDS pattern of NiO nanobelts.

This corroborates the formation of stoichiometric NiO nanobelts.

The UV–Vis spectroscopy was used to examine the optical properties of NiO nanobelts. The absorption spectra in Fig. 4 confirm the better absorbance of NiO nanobelts in the UV-Vis

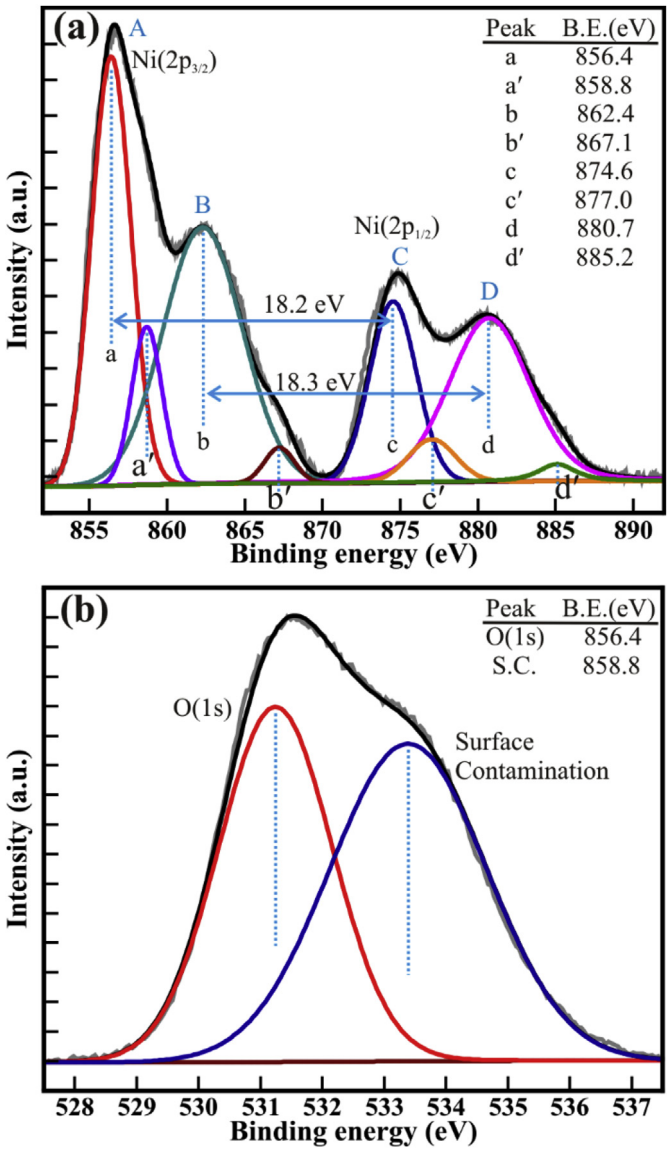

Fig. 3. High-resolution XPS spectra of the (a) Ni(2p), and (b) O (1s) core levels of the NiO nanobelts. The XPS spectra were deconvoluted via Voigt fitting function within Shirley background.

region. This absorption spectrum was further subjected to estimate the bandgap of NiO nanobelts using the equation [34].

$$(\alpha h\vartheta)^2 = A\,(h\vartheta - E_g) \tag{2}$$

where, hυ is the energy of a photon (≡ eV), A is a constant associated with the actual masses with the valence band and conduction band, α is the absorption coefficient (≡ cm^{-1}), and E_g is the bandgap of the NiO nanobelts (≡ eV). The bandgap of 4.07 eV was estimated from the plot of (hυ) versus $(\alpha h\upsilon)^2$. The reduced dimensions of the NiO nanobelts might be the reason for this increased bandgap than the bulk NiO (i.e., 3.68 eV) [26].

The photocatalytic activities of NiO nanobelts were performed to estimate the degradation of various organic dyes. The estimation of the optimum weight of the catalyst is essential to ensure the total absorption of efficient photons by avoiding ineffective excess of catalyst for the degradation of organic dyes. Therefore, the weight of NiO nanobelts was optimized for the photocatalytic degradation

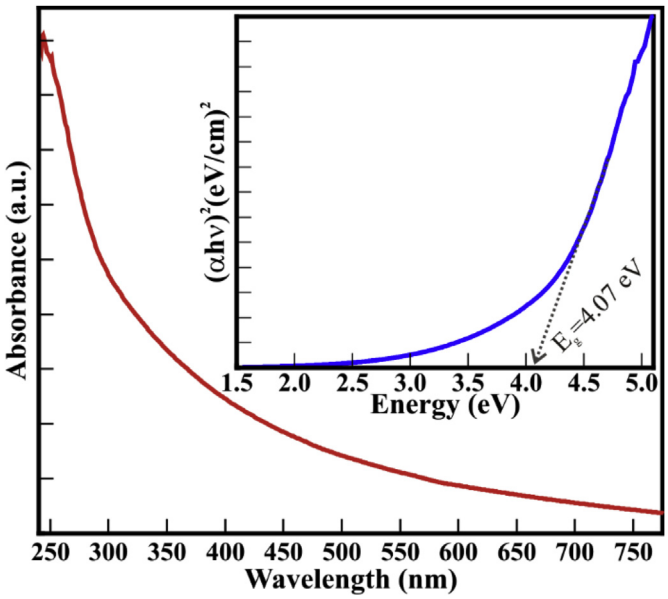

Fig. 4. UV–Visible absorption spectra of NiO nanobelt. The inset to figure shows the Tauc plot obtained from the absorption spectra.

of RhB dye, initially. Fig. 5 shows the UV–Vis spectra collected for photocatalytic activities of 25, 40, and 60 mg of NiO nanobelts on RhB dye. The RhB dye absorption band at 554 nm decreased gradually with continuous irradiation of 140 min for all concentrations of NiO nanobelts catalyst. However, the rate of reduction in its intensity has increased with an increase in the concentration of NiO nanobelts. The more significant reduction is observed for 60 mg of NiO. No extra peak/band observed after irradiation, terminate the evolution of derivative of NiO or RhB during the photocatalytic reaction. The degradation percentage as a function of time was estimated for each photocatalytic reaction with reference to maximum absorption at 554 nm.

Fig. 6 (a) shows the photocatalytic RhB degradation efficiency estimated from the UV–Vis spectra in Fig. 5. The maximum degradation efficiency evaluated for 25, 40, and 60 mg NiO nanobelts are 52.7, 65.8, and 89%, respectively. The highest RhB degradation efficiency observed for 60 mg of NiO is ascribed to the larger accessibility of electron-hole pairs in the reaction solution. The Langmuir-Hinshelwood model was applied to understand the kinetics of photocatalytic degradation reaction [35].

$$r = \frac{-dc}{dt} = \frac{kKC}{(1+KC)} \tag{3}$$

where, r is the rate of reaction (mol/L.min), C is the equilibrium concentration of the component (mol/L), t is the irradiation reaction time (min), K is the Langmuir constant (L/mol), and k is the rate constant (L/min). For the lesser concentration of catalyst, it can be simplified to the pseudo-first-order equation as

$$r = \frac{-Dc}{dt} = k_{obs}C \tag{4}$$

$$-\ln\frac{C_t}{C_o} = k_{obs}t \tag{5}$$

where, C_t and C_o are the dye concentrations (mol/L) at instants t and t = 0, respectively, t is the irradiation reaction time (min), and k_{obs} is the pseudo-first-order rate constant (L/min).

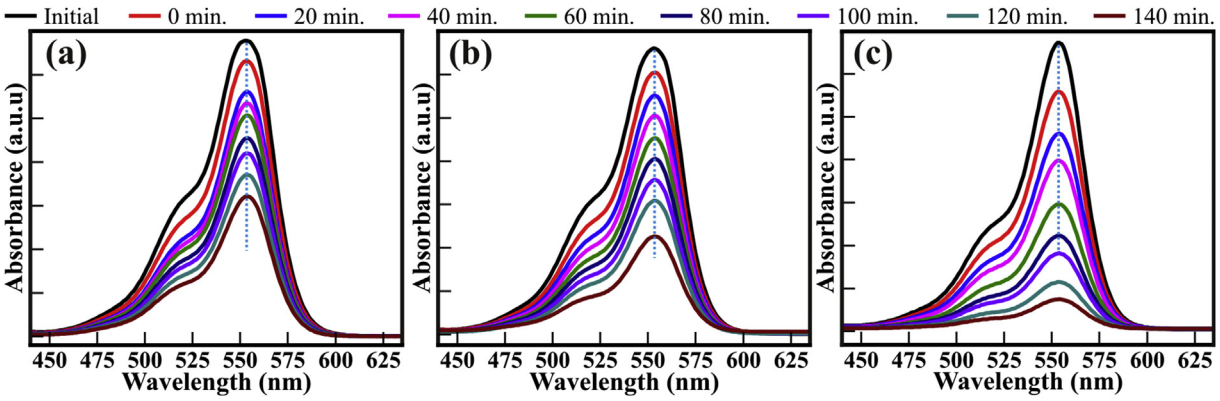

Fig. 5. UV–Visible absorption spectra of RhB dye solution collected at regular intervals for photocatalytic irradiation of 140 min in the presence of (a) 25, (b) 40, and (c) 60 mg NiO nanobelts.

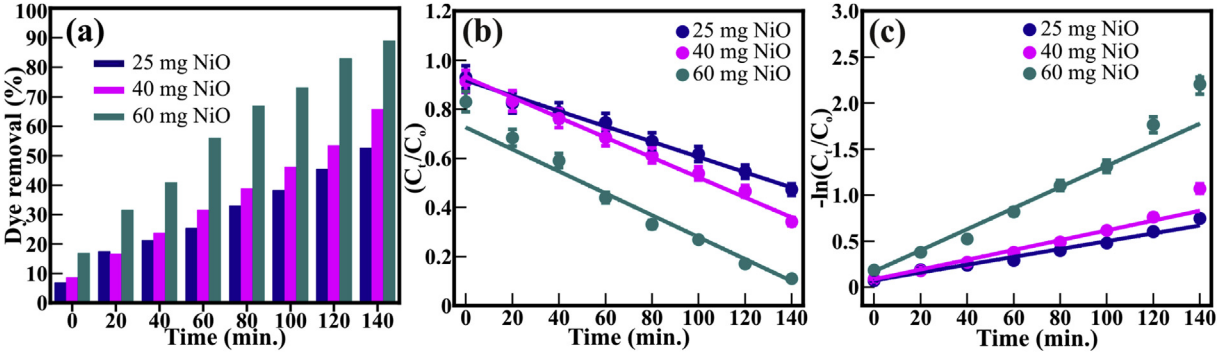

Fig. 6. (a) Histogram of degradation efficiency, and (b) kinetic curves and (c) corresponding pseudo-first-order kinetic plot evaluated for photocatalytically reduced RhB dye in the presence of NiO nanobelts at various irradiation time.

The reaction kinetics for the photocatalytic decolorization/degradation process is estimated from the graphs of C_t/C_o vs. irradiation reaction time (i.e., t), and -ln (C_t/C_o) vs. t. Fig. 6 (a and b) shows the effect of NiO catalyst on photocatalytic degradation kinetics of RhB dye solution. The degradation kinetics has improved with the concentration of NiO nanobelts. The rate constants (k) of 0.004, 0.006, and 0.012 min^{-1} was estimated for NiO nanobelts catalyst of 25, 40, and 60 mg, respectively. Moreover, the correlation coefficient (R^2) estimated was 0.98, 0.974, and 0.965, respectively. This confirms that 60 mg NiO catalyst performed well for the photocatalytic degradation of RhB dye. Therefore, 60 mg of NiO was utilized further to understand the degradation kinetics of other organic dyes such as MO, CV, and MB.

Fig. 7 shows the UV–Vis spectra of MO, CV, and MB dyes obtained at regular intervals after photocatalytic irradiation for continuous 140 min in the presence of 60 mg NiO. The maxima of absorption bands observed at 463, 590, and 664 nm are characteristics peak of MO, CV, and MB dyes, respectively. No other peak/band observed after irradiation, ruling out the formation of derivatives of dyes and NiO during the photocatalytic reactions. The irradiation time dependent reduction in the intensity of absorption maxima for all the dyes confirms their photocatalytic reduction. The degradation percentage was estimated for each photocatalytic reaction with reference to the respective maximum absorption.

The pseudo-first-order kinetic model describes the photocatalytic degradation processes. Fig. 8 (a & b) represents the plot of C_t/C_o and -ln (C_t/C_o) as a function of irradiation time (t) for the degradation of MO, CV, MB, and RhB dyes evaluated from Fig. 7. It confirmed that the photocatalytic degradation phenomenon fitted well with the pseudo-first-order kinetics. The rate constants (k) of 0.007, 0.008, 0.009, and 0.012 min^{-1} were evaluated for MO, MB, CV, and RhB, respectively. This indicates that the NiO nanobelts delivered a higher rate constant for RhB and lower rate constant for MO. Furthermore, the correlation coefficient (R^2) for MO, MB, CV, and RhB was 0.913, 0.923, 0.961, and 0.965, respectively. This illustrates the better response of NiO nanobelts for the photocatalytic removal of RhB and CV than that of MO and MB. Fig. 8(c) shows the histogram of the irradiation time dependent dye removal percentage estimated using maxima of absorption peaks observed at 463, 554, 590, and 664 nm for MO (Fig. 7(a)), RhB (Fig. 5(c)), CV (Fig. 7(b)), and MB (Fig. 7(c)). The 79.1, 82.7, 76.7, and 89% photocatalytic removal is observed at 140 min light irradiation for MO, CV, MB, and RhB dyes. This reveals that the NiO nanobelts have better photocatalytic reactivity towards RhB dyes. Moreover, the mesoporous NiO nanobelts comprising interlocked nanoparticles provided larger surface area, which might have formed excellent linkage with the dyes, and also absorbed larger amount photon, might be one of the reasons to provide better or compatible photocatalytic performance than various NiO nanostructures listed in the supporting information (i.e., Table S1).

FTIR studies were performed on pristine and photo-reacted NiO nanobelts to confirm the photocatalytic stability of Ni–O nanobelts. Fig. 9 shows the FTIR spectra of pristine NiO nanobelts, RhB adsorbed NiO nanobelts, and centrifugally extracted NiO nanobelts after the photocatalytic reaction. The FTIR spectra of pristine and centrifugally extracted (i.e., photo-reacted) NiO nanobelts are akin to each other and display the absorption peaks at 3429, 2921, 2849, 1634, 1468, 1382, 1269, 1020, 668, 569, and 471 cm^{-1}. These all

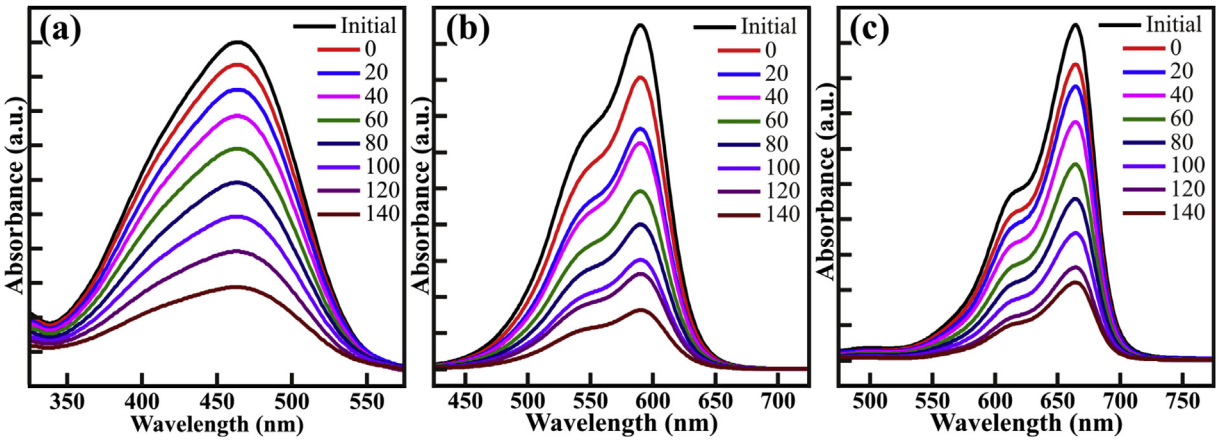

Fig. 7. Time-dependent UV–Visible absorption spectra of (a) MO, (b) CV, and (c) MB dye solutions collected at regular intervals for photocatalytic irradiation of 140 min in the presence of 60 mg NiO nanobelts.

absorption peaks are analogous to those reported for anodic arc plasma-treated NiO nanoparticles and heat-treated NiO films synthesized by electrodeposition [36,37]. However, the absorption of RhB dye on NiO nanobelts has resulted in two additional bands at 1130, and 1309 cm^{-1} are allotted to the stretching vibrational modes of *C—O—*C and *C*-aryl groups, respectively [38]. This confirms that the structural properties of NiO nanobelts have not chemically altered or not formed other organic compounds after loading of RhB dye and also during the photocatalytic process. Moreover, the stability of the NiO nanobelts in the photocatalytic reduction of organic dyes is confirmed from cyclic studies provided in the supporting information (Fig. S1). Thus, FTIR and stability studies revealed the highly stable photocatalytic cyclability of NiO nanobelts in the reduction of organic dyes.

Further insights into the formation of O_2^- radicals on the NiO surface, which play an important role in the degradation of the dyes was gained through state-of-the-art calculations based on the DFT, wherein the adsorption reactions between O_2 and NiO(110) surface was investigated. Before O_2 adsorption characterization, the electronic structure of NiO was determined (Fig. 10 (a & b)), predicting a bandgap of 3.76 eV for bulk NiO [25,26]. The partial density of states (PDOS) reveals that *O*-p states dominate the valence band, whereas Ni-d states dominate the conduction band edge. The lowest-energy O_2 adsorption geometries on the Ni(110) surface are shown in Fig. 10 (c & d). The adsorption energy for O_2 adsorbed side-on and end-on at Ni sites is calculated to be −3.59 and −1.62 eV, which indicates that the side-on O_2 configuration is energetically more favored than the end-on configurations. The O—O bond distance for O_2 bound in the side-on and end-on geometries is predicted at 1.360 and 1.278 Å, respectively, indicating elongation relative to the gas phase O_2 molecule (i.e., 1.24 Å). Bader population shows that the O_2 molecule gained −0.67 and 0.40 e^- when adsorbed in the side-on and end-on geometries, respectively, from the interacting surface Ni sites, resulting in the formation of O_2^- radicals. Atomic-level insights into the electron density redistribution within the O_2/NiO(110) system was obtained from the differential charge-density difference (Δρ) iso-surfaces analysis obtained by subtracting from the electron density of the total O_2/NiO(110) systems, both the electron density of the naked NiO(110) surface and that of the isolated O_2 molecule (i.e., $\Delta\rho = \rho_{O_2/NiO(110)} - \rho_{NiO(110)} - \rho_{O_2}$). The iso-surface contours reveal chemisorption of the O_2 molecule, characterized by electron density accumulation (cyan contours) within the newly formed Ni—O bonds and on the O_2 molecule, as shown in Fig. 10 (e & f). The formed O_2^- radicals on the NiO(110) surface are expected to react with the RhB dye, facilitating their degradation.

Furthermore, the influence of hydroxyl radicals (OH^-), superoxide radicals (O_2^-), and photogenerated holes (H^+) in the photodegradation of organic dyes was confirmed using distinct scavengers such as isopropanol (IPA), methanol (MeOH), and ammonium oxalate (AO), respectively [39]. The photocatalytic degradation of MB in the presence of IPA, MeOH, and AO (Fig. 11) showed the larger quenching in photodegradation of MB in the presence of AO. This confirmed the dominance of photogenerated H^+ species in the degradation process. A considerable reduction of the degradation efficiency in the presence of MeOH demonstrating the active role of O_2^-. Furthermore, a moderate reduction of degradation efficiency after using IPA indicates the partial involvement of OH^-. Overall, the O_2^-, and photogenerated H^+ from NiO nanobelts are significantly influencing the photodegradation of organic dyes. Fig. 12 represents the schematic mechanism of the photocatalytic activities for the dye degradation process using NiO nanobelts. The irradiation of NiO nanobelts during the degradation process transfers the photogenerated electrons (e^-) from the valence band (VB) to the conduction band (CB) while leaving holes (h^+) in VB. The holes either oxidize the pollutants/dyes directly or trapped by the hydroxyl group at the surface of catalysts to yield hydroxyl radicals (OH^-) [40]. The electrons from CB produce superoxide anion radicals (O_2^-) by reacting with a dissolved oxygen molecule and, after protonation, generate hydroperoxyl radicals (HO_2^-) [41]. These radicals decompose the pollutants/dyes in non-toxic products. Moreover, the bandgap of 4.07 eV and large surface area of NiO results in larger e^-—h^+ pairs generation. The photogenerated electron (e^-) – hole (h^+) pair control the photocatalytic activity of semiconducting materials. The higher recombination time of e^- and h^+ and larger interfacial electron transfer rates favor the enhancement of photocatalytic degradation efficiency [42]. Therefore, the following photocatalytic reactions are expected to happen at the surface of the NiO nanobelts.

$$NiO + h\vartheta \rightarrow NiO(e^- + h^+) \quad (6)$$

$$NiO(e^-) + O_2 \rightarrow NiO(O_2^-) \quad (7)$$

$$Dye + O_2^- \rightarrow Dye_{ox}(\text{intermediates}) \rightarrow CO_2\uparrow + H_2O \quad (8)$$

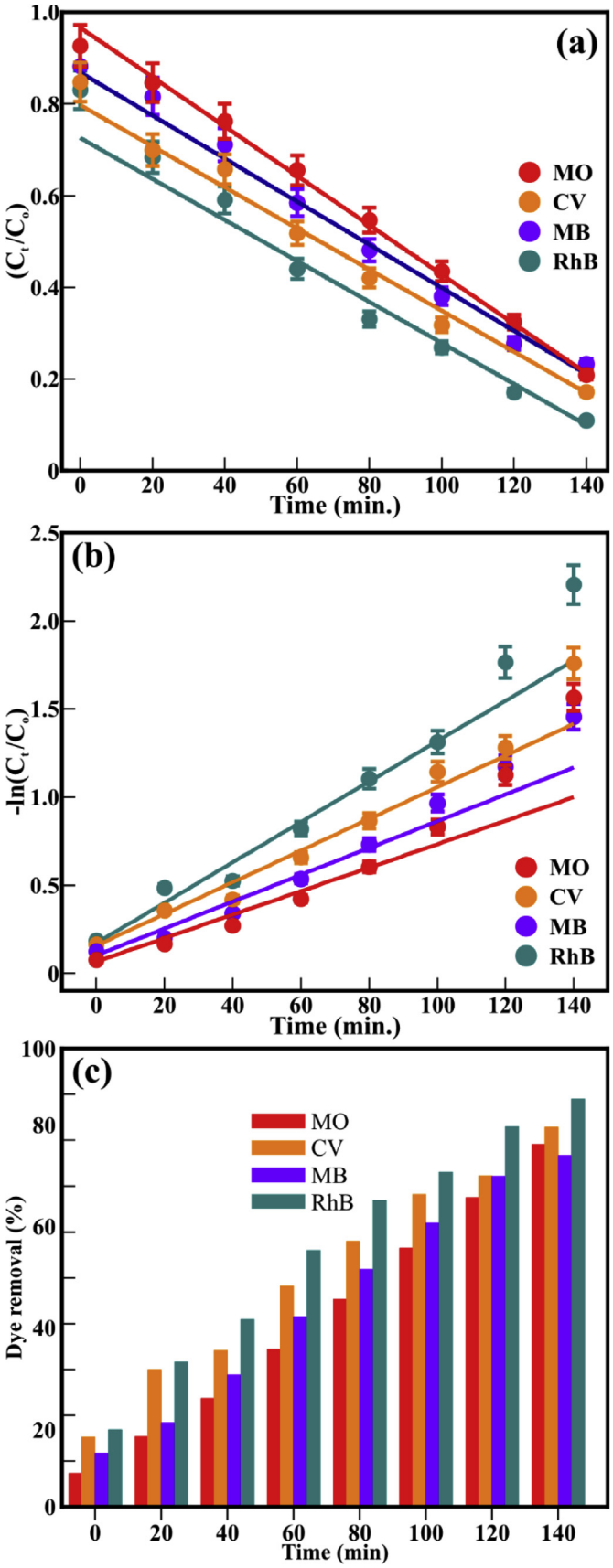

Fig. 8. (a) Kinetic curves and (b) corresponding pseudo-first-order kinetic plot, and (c) histogram of degradation efficiency evaluated for photocatalytically reduced MO, CV, MB, and RhB dyes in the presence of 60 mg NiO nanobelts at various irradiation time.

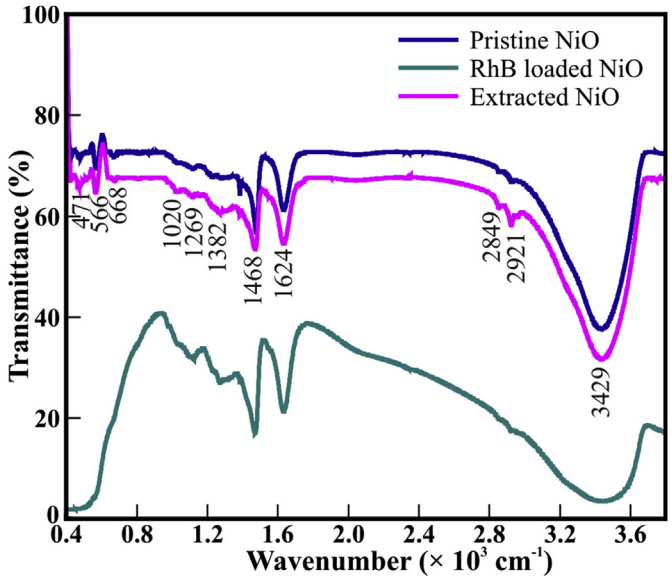

Fig. 9. FTIR spectra of pristine NiO nanobelts, RhB dye loaded NiO nanobelts, and NiO nanobelts extracted after photocatalytic degradation.

$$NiO(h^+) + H_2O \rightarrow NiO(OH^-) + H^+ \quad (9)$$

$$Dye + OH^- \rightarrow Dye_{ox}(intermediates) \rightarrow CO_2\uparrow + H_2O \quad (10)$$

where irradiation of solution with a photon of sufficient energy (i.e., $\geq E_{g(NiO)}$) generates e^- and h^+ in the VB and CB of NiO nanobelts, respectively (Eq. (6)). Further, NiO nanobelts reduce e^- and h^+ recombination by trapping e^- and enhance the formation of O_2^- radicals (eq. (7)) for the substantial degradation of the dyes (eq. (8)). Moreover, h^+ can react readily with H_2O and produce OH^- radicals (eq. (9)), which is an influential oxidizing agent capable of degrading most of the dye pollutants eventually into H_2O and CO_2 (eq. (10)). This analysis is akin to the theoretical predictions discussed above. Overall, well defined textural boundaries, perfect crystalline nature, larger accessible surface area, and 1D morphology of NiO nanobelts are the influencing factors in the improved photocatalytic degradation of organic pollutants.

4. Conclusion

In conclusion, NiO nanobelts synthesized using the hydrothermal technique were explored for photocatalytic degradation of various organic pollutants. The structural and morphological analysis confirmed the formation of cubic crystalline NiO nanobelts of thickness ~75 nm and a few micrometers in length. The bandgap of 4.07 eV for the NiO nanobelts was estimated from UV–Vis spectroscopy. The NiO nanobelts exhibited excellent photocatalytic activity for the removal of MO, MB, CV, and RhB organic dyes using a wide range of the spectrum. The optimized photocatalytic studies reveal the degradation efficiency of 79.1, 82.7, 76.7, and 89 % in 140 min for MO, MB, CV, and RhB, respectively, at the rate constants (k) of 0.007, 0.008, 0.009, and 0.012 min^{-1}. The NiO nanobelts delivered the best photocatalytic degradation efficiency for RhB than other organic dyes. Furthermore, the FTIR studies confirmed the stable chemical and photocatalytic properties of NiO nanobelts without the formation of other organic compounds after photocatalytic irradiation. The formation O_2^- radicals on the NiO(110) surface, as revealed from first-principles DFT calculations, is believed to facilitate the RhB dye degradation. The scavenging

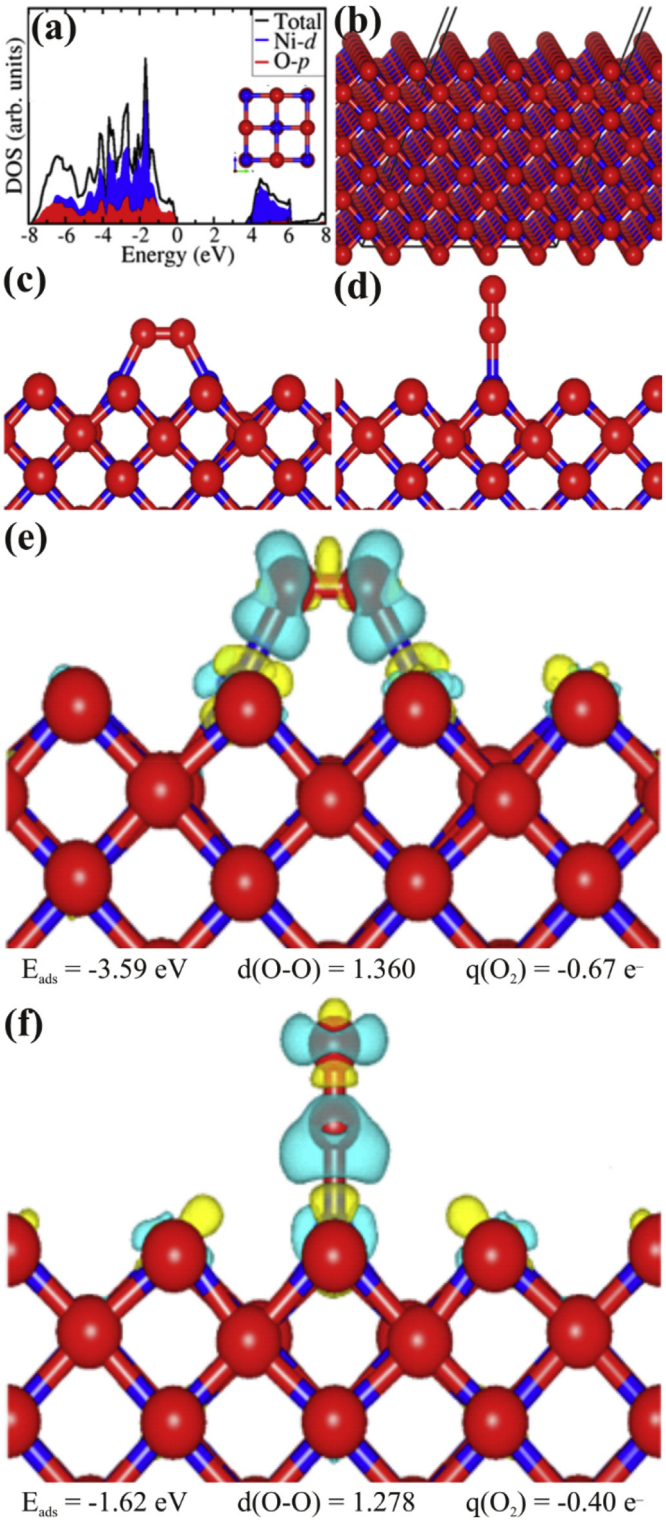

Fig. 10. (a) PDOS of rock salt NiO (inset), (b) optimized surface structure of NiO(110) surface. The relaxed adsorption structures of O_2 adsorbed in (c) side-on and (d) end-on configurations, with the corresponding differential charge density iso-surface contours (e & f), where the green and yellow contours indicate electron density increase and decrease by 0.003 e/Å^3, respectively. Blue and red atoms represent Ni and O, respectively. (For interpretation of the references to color in this figure legend, the reader is referred to the Web version of this article.)

studies confirmed the significant influence of the O_2^-, and photo-generated H^+ from NiO nanobelts in the photodegradation of organic dyes. Overall, these NiO nanobelts may be beneficial for the photocatalytic transformation of different chemicals and pollutants, in view of economic and environmentally friendly separation techniques.

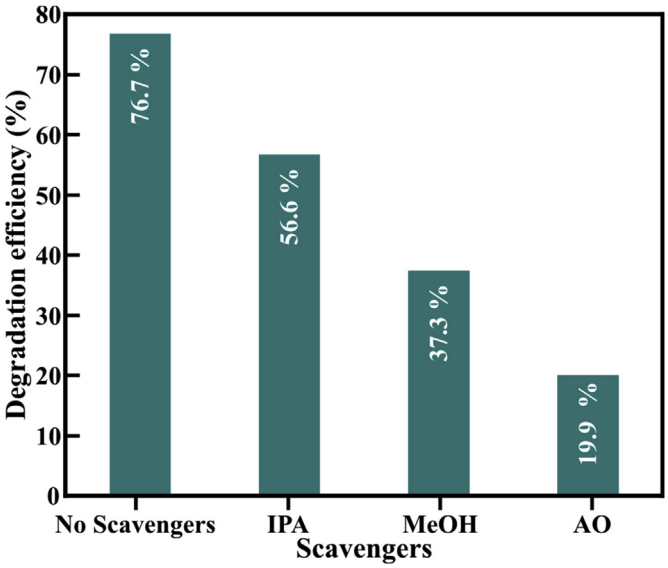

Fig. 11. Effect of distinct scavengers on the photocatalytic degradation of MB using NiO nanobelts.

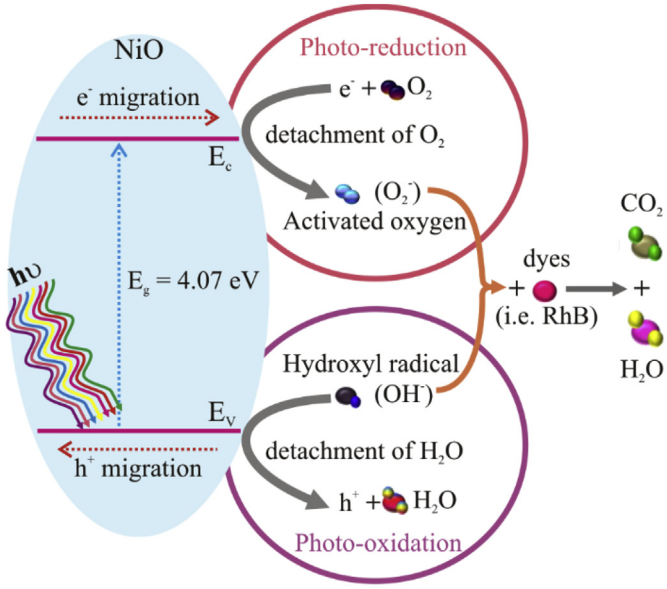

Fig. 12. Schematic of the photocatalytic degradation process of organic dyes using NiO nanobelts.

Declaration of competing interest

The authors declare that they have no known competing financial interests or personal relationships that could have appeared to influence the work reported in this paper.

Acknowledgment

The authors would like to thank UGC-DAE CSR Indore and SERB-DST India for their financial support to this research under grant No CSR—IC—BL-65/CRS-182/2017—18/189 and TAR/2019/000106,

respectively. SRR and NYD acknowledge the UK Engineering and Physical Sciences Research Council (EPSRC) for funding (Grant No. EP/S001395/1). This work has also used the computational facilities of the Advanced Research Computing, Cardiff (ARCCA) Division at Cardiff University and HPC Wales. This work also utilize the facilities of ARCHER (http://www.archer.ac.uk), the UK's national supercomputing service via the membership of the HEC Materials Chemistry Consortium funded by EPSRC (EP/L000202). Information on the data that underpins the results presented here, including how to access it, can be found in Cardiff University data catalogue at http://doi.org/10.17035/d.2020.0117383379.

Appendix A. Supplementary data

Supplementary data to this article can be found online at https://doi.org/10.1016/j.jallcom.2020.157337.

Credit Author Statement

RSD: Conceptualization, Methodology, Resources, Project administration, Visualization,
NRK, MSR: Synthesis of materials
NRK, MSR, SRM, MSP: Characterization
NRK and RSD: Analysis of results
SRR, RWC, NYD: DFT analysis
NRK and SRR: Writing original draft
NYD and RSD: Supervision, Funding acquisition, Writing-Review and editing

References

[1] K.-T. Chung, S.E. Stevens, C.E. Cerniglia, The reduction of azo dyes by the intestinal microflora, Crit. Rev. Microbiol. 18 (1992) 175–190, https://doi.org/10.3109/10408419209114557.
[2] M.-S. Chiou, P.-Y. Ho, H.-Y. Li, Adsorption of anionic dyes in acid solutions using chemically cross-linked chitosan beads, Dyes Pigments 60 (2004) 69–84, https://doi.org/10.1016/S0143.
[3] R. Vahini, P.S. Kumar, S. Karuthapandian, Bandgap-tailored NiO nanospheres: an efficient photocatalyst for the degradation of crystal violet dye solution, Appl. Phys. A 122 (2016) 744, https://doi.org/10.1007/s00339-016-0277-3.
[4] B. Cheng, Y. Le, W. Cai, J. Yu, Synthesis of hierarchical $Ni(OH)_2$ and NiO nanosheets and their adsorption kinetics and isotherms to Congo red in water, J. Hazard Mater. 185 (2011) 889–897, https://doi.org/10.1016/j.jhazmat.2010.09.104.
[5] J. Yang, B. Hou, J. Wang, B. Tian, J. Bi, N. Wang, X. Li, X. Huang, Nanomaterials for the removal of heavy metals from wastewater, Nanomaterials 9 (2019) 424, https://doi.org/10.3390/nano9030424.
[6] J. Kou, J. Gao, Z. Li, Z. Zou, Research on photocatalytic degradation properties of organics with different new photocatalysts, Curr. Org. Chem. 14 (2010) 728–744, https://doi.org/10.2174/138527210790963430.
[7] L. Gnanasekaran, R. Hemamalini, R. Saravanan, K. Ravichandran, F. Gracia, S. Agarwal, V.K. Gupta, Synthesis and characterization of metal oxides (CeO_2, CuO, NiO, Mn_3O_4, SnO_2 and ZnO) nanoparticles as photocatalysts for degradation of textile dyes, J. Photochem. Photobiol., B 173 (2017) 43–49, https://doi.org/10.1016/j.jphotobiol.2017.05.027.
[8] R.S. Devan, R.A. Patil, J.H. Lin, Y.R. Ma, One-dimensional metal-oxide nanostructures: recent developments in synthesis, characterization, and applications, Adv. Funct. Mater. 22 (2012) 3326–3370, https://doi.org/10.1002/adfm.201201008.
[9] A. Bhattacharjee, M. Ahmaruzzaman, CuO nanostructures: facile synthesis and applications for enhanced photodegradation of organic compounds and reduction of p-nitrophenol from aqueous phase, RSC Adv. 6 (2016) 41348–41363, https://doi.org/10.1039/C6RA03624D.
[10] X. Lou, J. Han, W. Chu, X. Wang, Q. Cheng, Synthesis and photocatalytic property of Co3O4 nanorods, Mater. Sci. Eng.: B 137 (2007) 268–271, https://doi.org/10.1016/j.mseb.2006.12.002.
[11] T.-H. Le, T.H.A. Ngo, V.T. Doan, L.M.T. Nguyen, M.C. Le, Preparation of manganese dioxide nanoparticles on laterite for methylene blue degradation, J. Chem. (2019), 1602752, https://doi.org/10.1155/2019/1602752.
[12] V. Manjunath, S. Bimli, K.H. Parmar, P.M. Shirage, R.S. Devan, Oxidized Nickel films as highly transparent HTLs for inverted planar perovskite solar cells, Sol. Energy 193 (2019) 387–394, https://doi.org/10.1016/j.solener.2019.09.070.
[13] D.S. Dalavi, R.S. Devan, R.S. Patil, Y.-R. Ma, P.S. Patil, Electrochromic performance of sol-gel deposited NiO thin film, Mater. Lett. 90 (2013) 60–63, https://doi.org/10.1016/j.matlet.2012.08.108.
[14] R.A. Patil, C.-P. Chang, R.S. Devan, Y. Liou, Y.-R. Ma, Impact of nanosize on supercapacitance: study of 1D nanorods and 2D thin-films of nickel oxide, ACS Appl. Mater. Interfaces 8 (2016) 9872–9880, https://doi.org/10.1021/acsami.6b00487.
[15] B. Liu, H. Yang, H. Zhao, L. An, L. Zhang, R. Shi, L. Wang, L. Bao, Y. Chen, Synthesis and enhanced gas-sensing properties of ultralong NiO nanowires assembled with NiO nanocrystals, Sensor. Actuator. B Chem. 156 (2011) 251–262, https://doi.org/10.1016/j.snb.2011.04.028.
[16] Y. Qiao, X.-S. Wu, C.M. Li, Interfacial electron transfer of Shewanella putrefaciens enhanced by nanoflaky nickel oxide array in microbial fuel cells, J. Power Sources 266 (2014) 226–231, https://doi.org/10.1016/j.jpowsour.2014.05.015.
[17] F. Motahari, M.R. Mozdianfard, F. Soofivand, M. Salavati-Niasari, NiO nanostructures: synthesis, characterization and photocatalyst application in dye wastewater treatment, RSC Adv. 4 (2014) 27654–27660, https://doi.org/10.1039/C4RA02697G.
[18] A. Khatri, P.S. Rana, Visible light photocatalysis of methylene blue using cobalt substituted cubic NiO nanoparticles, Bull. Mater. Sci. 42 (2019) 141, https://doi.org/10.1007/s12034-019-1835-z.
[19] H. Zeng, W. Cai, P. Liu, X. Xu, H. Zhou, C. Klingshirn, H. Kalt, ZnO-based hollow nanoparticles by selective etching: elimination and reconstruction of metal-semiconductor interface, improvement of blue emission and photocatalysis, ACS Nano 2 (2008) 1661–1670, https://doi.org/10.1021/nn800353q.
[20] S. Kant, D. Pathania, P. Singh, P. Dhiman, A. Kumar, Removal of malachite green and methylene blue by $Fe_{0.01}Ni_{0.01}Zn_{0.98}O$/polyacrylamide nanocomposite using coupled adsorption and photocatalysis, Appl. Catal. B Environ. 147 (2014) 340–352, https://doi.org/10.1016/j.apcatb.2013.09.001.
[21] G. Kresse, J. Furthmüller, J. Hafner, Theory of the crystal structures of selenium and tellurium: the effect of generalized-gradient corrections to the local-density approximation, Phys. Rev. B 50 (1994) 13181–13185, https://doi.org/10.1103/PhysRevB.50.13181.
[22] P.E. Blöchl, Projector augmented-wave method, Phys. Rev. B 50 (1994) 17953–17979, https://doi.org/10.1103/PhysRevB.50.17953.
[23] J.P. Perdew, K. Burke, M. Ernzerhof, Generalized gradient approximation made simple (vol 77, pg 3865, 1996), Phys. Rev. Lett. 78 (1997) 1396, https://doi.org/10.1103/PhysRevLett.78.1396.
[24] S. Grimme, J. Antony, S. Ehrlich, H. Krieg, A consistent and accurate ab initio parametrization of density functional dispersion correction (DFT-D) for the 94 elements H-Pu, J. Chem. Phys. 132 (2010), 154104, https://doi.org/10.1063/1.3382344.
[25] J.Y. Zhang, W.W. Li, R.L.Z. Hoye, J.L. MacManus-Driscoll, M. Budde, O. Bierwagen, L. Wang, Y. Du, M.J. Wahila, L.F.J. Piper, T.L. Lee, H.J. Edwards, V.R. Dhanak, K.H.L. Zhang, Electronic and transport properties of Li-doped NiO epitaxial thin films, J. Mater. Chem. C 6 (2018) 2275–2282, https://doi.org/10.1039/C7TC05331B.
[26] R.A. Patil, R.S. Devan, J.-H. Lin, Y. Liou, Y.-R. Ma, An efficient methodology for measurement of the average electrical properties of single one-dimensional NiO nanorods, Sci. Rep. 3 (2013) 3070, https://doi.org/10.1038/srep03070.
[27] A.V. Krukau, O.A. Vydrov, A.F. Izmaylov, G.E. Scuseria, Influence of the exchange screening parameter on the performance of screened hybrid functionals, J. Chem. Phys. 125 (2006), 224106, https://doi.org/10.1063/1.2404663.
[28] G.W. Watson, E.T. Kelsey, N.H. de Leeuw, D.J. Harris, S.C. Parker, Atomistic simulation of dislocations, surfaces and interfaces in MgO, J. Chem. Soc. Faraday Trans. 92 (1996) 433–438, https://doi.org/10.1039/FT9969200433.
[29] W. Tang, E. Sanville, G. Henkelman, A grid-based Bader analysis algorithm without lattice bias, J. Phys. Condes. Matter 21 (2009), 084204, https://doi.org/10.1088/0953-8984/21/8/084204.
[30] N. Kitchamsetti, P.R. Chikate, R.A. Patil, Y.-R. Ma, P.M. Shirage, R.S. Devan, Perforated mesoporous NiO nanostructures for enhanced pseudocapacitive performance with ultra-high rate capability and high energy density, CrystEngComm 21 (2019) 7130–7140, https://doi.org/10.1039/C9CE01475F.
[31] N. Kitchamsetti, R.S. Kalubarme, P.R. Chikate, C.J. Park, Y.R. Ma, P.M. Shirage, R.S. Devan, An investigation on the effect of Li-ion cycling on the vertically aligned brookite TiO_2 nanostructure, Chemistry 4 (2019) 6620–6626, https://doi.org/10.1002/slct.201900395.
[32] P.R. Chikate, P.K. Bankar, R.J. Choudhary, Y.-R. Ma, S.I. Patil, M.A. More, D.M. Phase, P.M. Shirage, R.S. Devan, Spitzer shaped ZnO nanostructures for enhancement of field electron emission behaviors, RSC Adv. 8 (2018) 21664–21670, https://doi.org/10.1039/C8RA03282C.
[33] D.S. Dalavi, R.S. Devan, R.S. Patil, Y.-R. Ma, M.-G. Kang, J.-H. Kim, P.S. Patil, Electrochromic properties of dandelion flower like nickel oxide thin films, J. Mater. Chem. 1 (2013) 1035–1039, https://doi.org/10.1039/C2TA00842D.
[34] X. Wan, M. Yuan, S.L. Tie, S. Lan, Effects of catalyst characters on the photocatalytic activities of NiO nanoparticles in the degradation of methylene blue, Appl. Surf. Sci. 277 (2013) 40–46, https://doi.org/10.1016/j.apsusc.2013.03.126.
[35] A. Kubiak, K. Siwińska-Ciesielczyk, Z. Bielan, A. Zielińska-Jurek, T. Jesionowski, Synthesis of highly crystalline photocatalysts based on TiO_2 and ZnO for the degradation of organic impurities under visible-light irradiation, Adsorption 25 (2019) 309–325, https://doi.org/10.1007/s10450-019-00011-x.
[36] Z. Wei, H. Qiao, H. Yang, C. Zhang, X. Yan, Characterization of NiO nanoparticles by anodic arc plasma method, J. Alloys Compd. 479 (2009) 855–858, https://doi.org/10.1016/j.jallcom.2009.01.064.
[37] F. Basharat, U. Rana, M. Shahid, M. Serwar, Heat treatment of electrodeposited NiO films for improved catalytic water oxidation, RSC Adv. 5 (2015)

86713–86722, https://doi.org/10.1039/C5RA17041A.
[38] N. Mchedlov-Petrossyan, S. Shapovalov, S. Egorova, V. Kleshchevnikova, E.A. Cordova, A new application of rhodamine 200 B (Sulfo rhodamine B), Dyes Pigments 28 (1995) 7–18, https://doi.org/10.1016/0143-7208(94)00058-A.
[39] N. Li, Y.L. He, J.J. Lian, Q.G. Liu, X.X. Zhang, X. Zhang, Facile fabrication of a NiO/Ag_3PO_4 Z-scheme photocatalyst with enhanced visible-light-driven photocatalytic activity, New J. Chem. 44 (2020) 12806–12814, https://doi.org/10.1039/d0nj01060j.
[40] K. Hayat, M. Gondal, M.M. Khaled, S. Ahmed, Effect of operational key parameters on photocatalytic degradation of phenol using nano nickel oxide synthesized by sol-gel method, J. Mol. Catal. Chem. 336 (2011) 64–71, https://doi.org/10.1016/j.molcata.2010.12.011.
[41] L.G. Devi, N. Kottam, B.N. Murthy, S.G. Kumar, Enhanced photocatalytic activity of transition metal ions Mn^{2+}, Ni^{2+} and Zn^{2+} doped polycrystalline titania for the degradation of Aniline Blue under UV/solar light, J. Mol. Catal. Chem. 328 (2010) 44–52, https://doi.org/10.1016/j.molcata.2010.05.021.
[42] D. Chatterjee, S. Dasgupta, Visible light induced photocatalytic degradation of organic pollutants, J. Photochem. Photobiol. C Photochem. Rev. 6 (2005) 186–205, https://doi.org/10.1016/j.jphotochemrev.2005.09.001.